96 KSME International Journal, Vol. 11, No. 1, pp. 96~105, 1997

Unsteady Shock Waves in Supersonic Nozzles

Min-Gyoo Lee*, Jong-Ho Park* and Michio Nishida**

(Received April 26, 1996)

The present paper describes the numerical and experimental results on unsteady nozzle flows induced by nonstationary shock waves. The two-dimensional Navier-Stokes equations are numerically solved using the upwind TVD finite-difference scheme of the Harten-Yee type. For the purpose of computational visualization of shock waves in transient nozzle starting process, computer shadowgraphs are developed based on the principle of the optical shadowgraph. Visualization experiments employing a conventional shock tube are also performed. Comparison of numerical and experimental results shows satisfactory agreement. Furthermore, the steady flow establishment process around an airfoil model installed inside the nozzle is numerically investigated. The simulated results successfully reveal the unsteady viscous flow structure around the model.

Key Words: Fluid Dynamics, Unsteady Flow, Shock Wave, Nozzle, Shock Tube, Computational Fluid Dynamics, Upwind TVD Scheme, Navier-Stokes Equations

1. Introduction

Recently there has been renewed interest in impulse-type high-enthalpy aerodynamic facilities as a means of providing hypersonic flow conditions. Reflected-type shock tunnels have been one of the most successful types of hypersonic impulse test facilities that can economically produce hypersonic flows. Therefore, these shock tunnels have been used successfully in various aerodynamic experiments(Takeishi et al 1994). As a variation of a shock tube, the expansion of a gas behind an incident shock wave travelling through a non-reflected divergent nozzle was first employed to generate hypersonic flows by Hertzberg. (1951) However, the starting process in the nozzle of such a simple expansion mode leads to a reduction in flow duration. Thereafter Wittliff et al.(1959) proposed a new operation technique of a reflection mode that uses a high-temperature and high-pressure gas behind the shock wave reflected from the shock tube end wall as reservoir gas, whereby the flow duration is increased much more than that in the expansion mode.

The principal problem regarding hypersonic shock tunnels is the so-called steady flow establishment time and duration because of their extremely short running time for aerodynamic experiments. For example, the typical duration of the quasi-steady flow is of the order of a few milliseconds. Therefore the starting process of shock tunnels is an important and interesting problem.

Concerning the starting process of a hypersonic nozzle, Smith(1966) analytically and experimentally studied a shock propagation problem. Amann and Reichenbach(1973), and Ikui and Matsuo(1971) also experimentally investigated the behavior of the shock waves in several two-dimensional nozzles by means of an optical Schlieren technique. Holden(1971) conducted experiments with an aerodynamic model at the nozzle exit and proposed an experimental formula to estimate the flow establishment time around an

* Department of Mechanical Engineering, Chungnam National University, Taejon 305-764, Korea.

** Department of Aeronautics and Astronautics, Kyushu University, Fukuoka 821-81, Japan.

aerodynamic model.

Using the random choice method (RCM), Kashimura et al.(1986) numerically analyzed wave propagation in a Laval nozzle and a Ludwieg tube, and their treatment was quasi-one-dimensional. With the rapid development of computation environment and numerical methods, the multi-dimensional computations of the nozzle starting process have been conducted by several researchers. Recently, Jacobs(1992) numerically simulated the starting process in an axisymmetric nozzle. Prodromou and Hiller(1992) also conducted a numerical simulation using the Godunov-type scheme and compared their numerical solutions with the experimental results shown by Amann and Reichenbach(1973). We have also calculated the nozzle stating process taking into consideration on the bursting of a secondary diaphragm and the high-temperature effects.(Lee and Nishida, 1992, 1993, 1994) In the present work, our previous computational work(Lee and Nishida, 1992) of shock wave propagation in a nozzle using an inviscid flow model is extended to a viscous flow treatment. Thereby, viscous effects, such as the interaction of a secondary shock with a wall boundary layer and the separation of the nozzle flow, can be investigated. In addition, visualization experiments using a conventional shock tube are performed and comparisons between computer shadowgraphs and experimental ones are made. Furthermore, the transient process around an airfoil model installed inside the nozzle is numerically investigated.

2. Governing Equations and Numerical Procedures

2.1 Governing equations

The flow model considered here is such that a shock wave travels to the right-hand side of a shock tube and then enters a nozzle connected to the end of the shock tube as shown in Fig. 1. Air is considered as working gas and the flow induced by the shock wave is treated as viscous. A two-dimensional flow is treated here for comparison with the experiments which were carried out

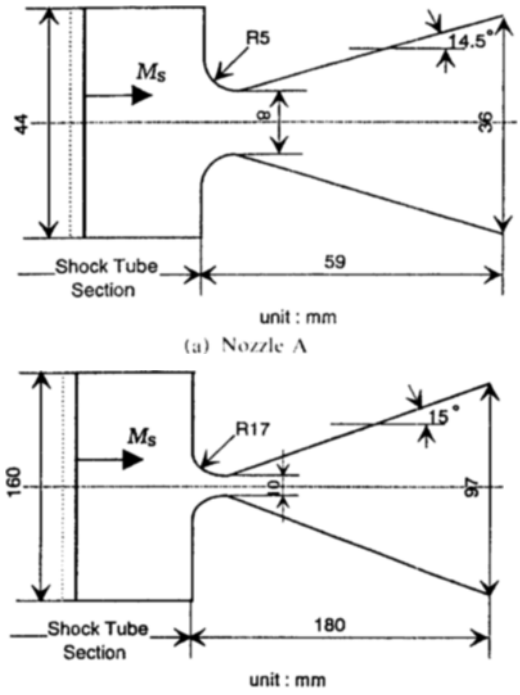

Fig. 1 Geometry of convergent-divergent nozzles, nozzle *A* and *B*

in two-dimensional flow. Therefore, the governing equations are the two-dimensional Navier-Stokes equations in the generalized coordinate (ξ, η, τ).

$$\frac{\partial \hat{\boldsymbol{q}}}{\partial \tau}+\frac{\partial \hat{\boldsymbol{F}}}{\partial \xi}+\frac{\partial \hat{\boldsymbol{G}}}{\partial \eta}=\frac{1}{Re}\left(\frac{\partial \hat{\boldsymbol{F}}_v}{\partial \xi}+\frac{\partial \hat{\boldsymbol{G}}_v}{\partial \eta}\right) \quad (1)$$

where $\hat{\boldsymbol{q}}$ is a conservative variable, $\hat{\boldsymbol{F}}$ and $\hat{\boldsymbol{G}}$ denote the flux vectors in the ξ- and η-directions, respectively, and $\hat{\boldsymbol{F}}_v$ and $\hat{\boldsymbol{G}}_v$ are the viscous terms in the ξ-and η-directions, respectively. The Reynolds number Re is given by $\rho_1 a_1 L/\mu_1$ and the subscript 1 indicates the state in front of an incident shock wave. The components of the aforementioned vectors are as follows(H. C. Yee 1989):

$$\hat{\boldsymbol{q}}=J^{-1}[\rho,\ \rho u,\ \rho v,\ E]^T \quad (2)$$

$$\hat{\boldsymbol{E}}=J^{-1}[\rho U,\ \rho uU+\xi_x p,\ \rho vU+\xi_y p,\ (E+p)\ U-\xi_t p]^T \quad (3)$$

$$\hat{\boldsymbol{F}}=J^{-1}[\rho V,\ \rho uV+\eta_x p,\ \rho vV+\eta_y p,\ (E+p)\ V-\eta_t p]^T \quad (4)$$

$$\hat{\boldsymbol{F}}_v=J^{-1}[0,\ \xi_x\tau_{xx}+\xi_y\tau_{xy},\ \xi_x\tau_{yx}+\xi_y\tau_{yy},\ \xi_x f_4+\xi_y g_4]^T \quad (5)$$

$$\hat{\boldsymbol{G}}_v = J^{-1}[0,\ \eta_x\tau_{xx}+\eta_y\tau_{xy},\ \eta_x\tau_{yx}+\eta_y\tau_{yy},\ \eta_x f_4+\eta_y g_4]^T \quad (6)$$

$$p=(\gamma-1)\left[E-\rho(u^2+v^2)/2\right] \quad (7)$$

where t is time, p pressure, ρ density and $\boldsymbol{E}$ total energy per unit volume. u and v are the velocity components in the x- and y-directions, respectively, and

$$\tau = t \quad (8)$$

$$J=\xi_x\eta_y-\xi_y\eta_x \quad (9)$$

$$U=\xi_t+\xi_x u+\xi_y v \quad (10)$$

$$V=\eta_t+\eta_x u+\eta_y v \quad (11)$$

Here, J is the transform Jacobian, and U and V are the contravariant velocity components in a computational domain.

The components of the viscous vectors are as follows :

$$\tau_{xx}=\mu(4u_x-2v_y)/3 \quad (12)$$

$$\tau_{xy}=\tau_{yx}=\mu(u_y+v_x) \quad (13)$$

$$\tau_{yy}=\mu(-2u_x+4v_y)/3 \quad (14)$$

f_4 and g_4 are defined as

$$f_4=u\tau_{xx}+v\tau_{xy}+\mu(\gamma-1)^{-1}\mathrm{Pr}^{-1}(a^2)_x \quad (15)$$

$$g_4=u\tau_{yx}+v\tau_{yy}+\mu(\gamma-1)^{-1}\mathrm{Pr}^{-1}(a^2)_y \quad (16)$$

where the viscous coefficient μ is evaluated from Sutherland's semi-empirical formula and subscripts x and y imply $\partial/\partial x$ and $\partial/\partial y$, respectively. The speed of sound is denoted by a and the Prandtl number is set to $\mathrm{Pr}=0.72$. In the above equations, the variables are nondimensionalized using the properties in front of an incident shock wave. The vertical length measured from the central surface of a shock tube is selected as the reference length scale.

2.2 The numerical methods

The numerical method for spatial discretization employs the second-order upwind TVD scheme of the Harten-Yee type that can satisfactorily capture discontinuities with less numerical smearing. The notion of the stable TVD scheme was introduced by Harten(1983). It was originally proposed for a scalar hyperbolic partial differential equation, based on the condition (TVD condition) sufficient for the stability of numerical solutions. In the present work, we adopt the Harten-Yee upwind non-MUSCL TVD scheme that uses the linearized Riemann solver of the Roe(1981) type. The viscous and dissipation terms appearing on the right-hand side of the governing equation are treated by a conventional second-order central difference technique. The details on numerical procedures can be found in Lee(1995).

The second-order time integration by the explicit fractional step technique is employed, because the time accurate solutions are sought to calculate actual unsteady flowfield under consideration. The difference operators for each spatial term and nonhomogeneous term of governing Eq. (1) are split as follows:

$$L_\xi:\ \frac{\partial\hat{\boldsymbol{q}}}{\partial\tau}+\frac{\partial\hat{\boldsymbol{F}}(\hat{\boldsymbol{q}})}{\partial\xi}=0 \quad (17)$$

$$L_\eta:\ \frac{\partial\hat{\boldsymbol{q}}}{\partial\tau}+\frac{\partial\hat{\boldsymbol{G}}(\hat{\boldsymbol{q}})}{\partial\eta}=0 \quad (18)$$

$$L_s:\ \frac{\partial\hat{\boldsymbol{q}}}{\partial\tau}=\frac{1}{Re}\left(\frac{\partial\hat{\boldsymbol{F}}_v}{\partial\xi}+\frac{\partial\hat{\boldsymbol{G}}_v}{\partial\eta}\right) \quad (19)$$

The time integration formula using the above operators can be expressed as

$$\hat{\boldsymbol{q}}_{i,j}^{n+2}=L_\xi^h L_\eta^h L_s^h L_s^h L_\eta^h L_\xi^h\ \hat{\boldsymbol{q}}_{i,j}^{n} \quad (20)$$

where $h=\Delta\tau$, n is the time step, and L_ξ^h, L_η^h, L_s^h, denote operators for the ξ- and η-directions and the viscous term, respectively.

2.3 Initial and boundary conditions

As shown in Fig. 1, the flow is symmetric along the axis, so that only the upper half of the flowfield is taken into account. Elliptic partial differential equations (Poisson equation) are used to generate a body-oriented grid system and are solved by a standard Poisson solver, that is, a successive overrelaxation (SOR) method(Steger and Sorenson,1979). As the computational grid systems for nozzle A, two single-block grids with 300×50 and 360×60 grid points are used. The first one is for the unsteady nozzle flow computation without an aerodynamic model and the other one is for the case with a model installed inside the nozzle.

An incident shock wave is set initially in the left boundary of the computational domain. The initial distributions of the flow properties are given by the shock jump conditions. No-slip and adiabatic conditions are imposed on the wall of a

shock tube and a nozzle. Symmetric conditions are imposed on the central line and the inflow-outflow conditions are given on the left and right sides.

3. Experimental Method

In order to validate the numerically calculated results, experiments on the shock propagation problem in a nozzle were carried out using a conventional shock tube with air as the driver and driven gases. The driver and driven sections are 270 cm and 370 cm in length, respectively. The cross section of the measurement section is a square of 4.4 cm × 4.4 cm. The arrangement of the apparatus for visualization experiment is shown in Fig. 2. Optical shadowgraph pictures were taken at an incident shock wave of M_s=2.2. The nano-spark 1400 (Miyashiro et al.,1992) was used as light source for the optical system. Because the flash time of the nano-spark is approximately 50 ns, it is appropriate for the present high-speed phenomenon.

The initial pressure in the driven section was set to $p_1=6.5\times10^3$ Pa, and the driver section pressure was set to $p_4=5.1\times10^5$ Pa to produce incident shock waves with M_s=2.2. Incident shock speeds have been measured by time of flight between two the piezo electric pressure sensors (PCB model 131A21), that distance is 239mm close to the end of the low pressure tube. Signals from each pressure tranducers input to storagescope(Tektronix Model 7623A) and then saved in personal computer.

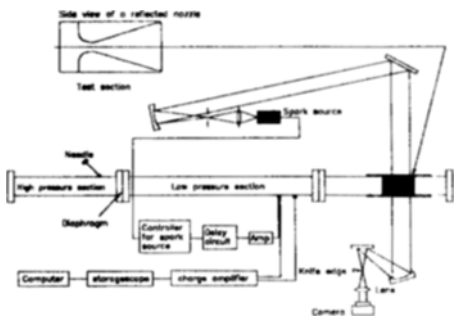

Fig. 2 Experimental setup

4. Results and Discussion

4.1 Unsteady staring process in a nozzle *A*

The present numerical calculations were conducted for moving shock waves of M_s=2.2 and 3.2 traveling initially in the low pressure section of a shock tube with $p_1=6.5\times10^3$ Pa, and $T_1=288$ K. The Reynolds number is 3.3×10^4. For a two-dimensional flow, the contrast of the optical shadowgraphs is proportional to $\Delta\rho$(Δ: Laplacian). We calculated the quantities of $\Delta\rho$ from numerical data on all grid points for the purpose of computational visualization of unsteady shock waves in the starting process. Thus shadowgraphs were generated on a computer based on the principle of the optical shadowgraph. This may be referred to as computer shadowgraph. Thus produced computer shadow-

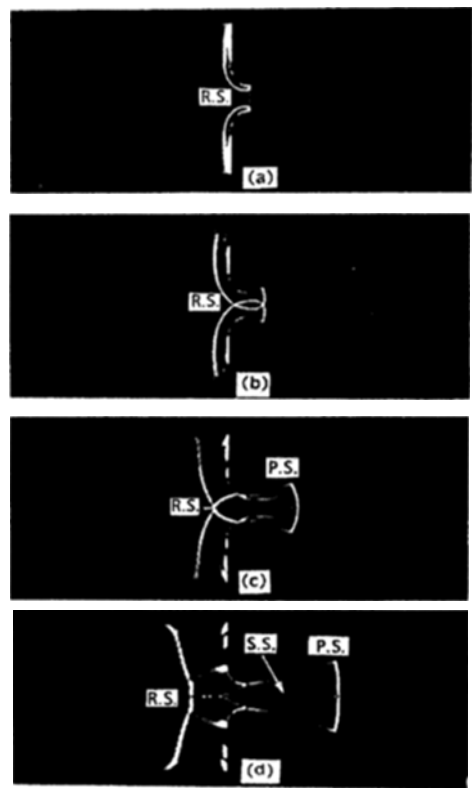

Fig. 3 Continued

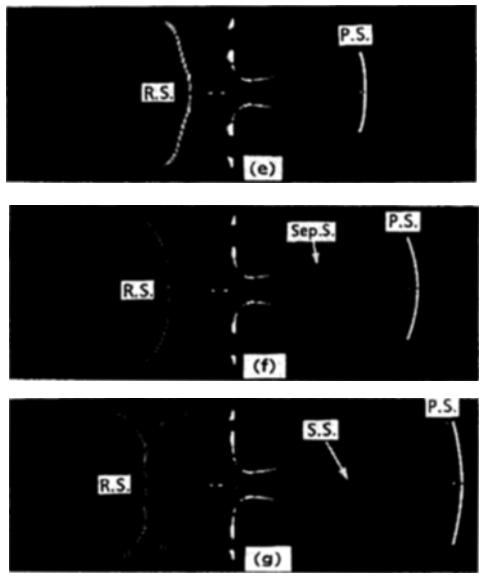

Fig. 3 Computer shadowgraphs showing transient flows in a nozzle A, $M_s=2.2$, (a) $t'=1.32$ (b) $t'=1.42$ (c) $t'=1.63$ (d) $t'=1.90$ (e) $t'=2.21$ (f) $t'=2.32$ (g) $t'=2.62$

graphs are presented in Fig. 3. Though optical shadowgraphs and Schlieren pictures are usually compared with density contours drawn from numerical results, we consider that employment of computer shadowgraphs would be more appropriate for qualitative comparison with experimental results. One can understand from the figure that the dark side of the wave is facing the propagation direction, specifically it denotes the low density side.

The time given in Fig. 3 is nondimensional, namely $t'=ta_1/L$, where L is the vertical length of the shock tube measured from the centerline and a_1 is the speed of sound in front of the incident shock wave. The incident shock wave propagates from the left side of the figure. One of the present research objectives is to obtain the fundamental knowledge of the shock wave propagation behavior from the shock tube section to the nozzle section; thus we do not consider a secondary diaphragm that is usually mounted in actual shock tunnels. At first ((a): $t'=1.32$), the upper and lower portions of the incident shock wave are partially reflected from the shock tube end wall and the rest portion propagates into the nozzle. The shock wave reflected from the nozzle throat exhibits a Mach reflection. After some time, the shock wave reflected from the upper throat and that reflected from the lower throat intersect at the central surface and propagate upstream. The blot image in front of the reflected shock wave (R.S.) is not physical and it is numerical, namely, it is due to a decrease in numerical accuracy, because the numerical accuracy at the boundary on the axis is decreased to the first order and the grid interval is relatively coarse compared to that of the wall.

In Fig. 3(c), the front of the primary shock wave (P.S.) propagating in the nozzle becomes a curved, smooth front. At $t'=1.90$ (Fig. 3(d)), a secondary shock wave (S.S.) is observed.

There is a difference in pressure, which is high behind the primary shock wave and low in the gas expanded through the nozzle throat. Thereby, a secondary shock wave is generated by the pressure difference. The left-hand side of the secondary shock wave is dark, which indicates that the secondary shock wave is upstream-facing (left-facing). However, the secondary shock wave is propagated by a supersonic flow expanded from the nozzle throat. Therefore, as shown in Figs. 3(e) to (g), the speed of the secondary shock wave is low compared with that of the primary shock wave. After the secondary shock wave reaches the nozzle exit, a steady supersonic flow can be obtained at the exit. The interaction between the upstream-facing secondary shock wave and the wall boundary layer results in the flow separation from the wall, and a separation shock wave(Sep.S.) is formed that is well resolved in the numerical results (Fig. 3(d) to(g)).

Figure 4 shows the time course of the density distribution on the nozzle axis. The nozzle throat is placed at $x/L=2.98$. The letters in the figure denote a: $t'=1.32$, b: $t'=1.63$, c: $t'=2.02$, d: $t'=2.32$, e: $t'=2.62$. At $t'=1.32$, the flow properties on the axis is not affected by the reflected shock wave and are determined by the jump condition of the incident shock wave (primary shock wave). Therefore, the density behind the primary shock wave in the nozzle is the same as

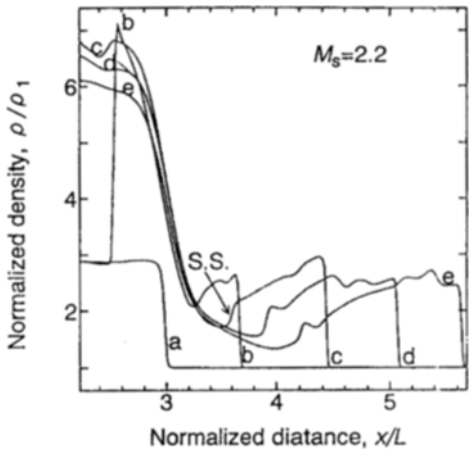

Fig. 4 On-axis density distributions, M_s = 2.2

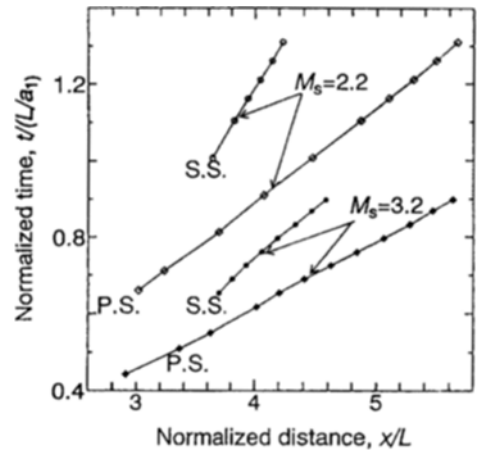

Fig. 5 Propagation trajectories of primary and secondary shock wave, M_s = 2.2, 3.2

that behind the incident shock wave (see Fig. 3(a)). We can identify the secondary shock wave (S.S.) from the density distribution at t'=2.02. Because the gas behind the reflected shock wave is expanded into the nozzle, it can be understood from the density distribution that the density behind the reflected shock wave decreases with time.

The calculation using another shock Mach number was also carried out to investigate the effect of the incident shock strength on the shock wave propagation behavior within the nozzle. The incident shock Mach number of M_s = 3.2 is used for this investigation. The trajectories of the primary (P.S.) and secondary shock waves (S.S.) are plotted in Fig. 5. The primary and secondary shock waves propagate at nearly constant velocity. As expected, the propagation velocity of the primary and secondary shock waves increases with an increase in the incident shock strength. Furthermore, the propagation velocity of the secondary shock wave is slightly more sensitive to the strength of the incident shock wave compared with that of the primary shock wave.

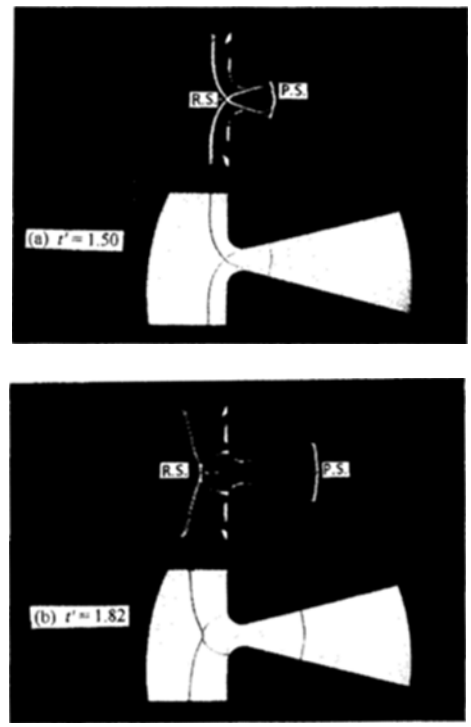

Fig. 6 Comparison between computational and experimental shadowgraphs. (a) t' = 1.50, upper: computational, lower: experimental (b) t' = 1.82, upper: computational, lower: experimental

In Fig. 6, the comparisons between the computational and experimental shadowgraphs are shown. The times given in the figure are those in the numerical simulation. Satisfactory agreement between the numerical and experimental results is obtained. Hence the numerical simulation successfully predicts the shock wave propagation behavior in an unsteady starting process. The physical time interval between Fig. 6(a) and Fig. 6(b) is 0.025msec. The time in a computational

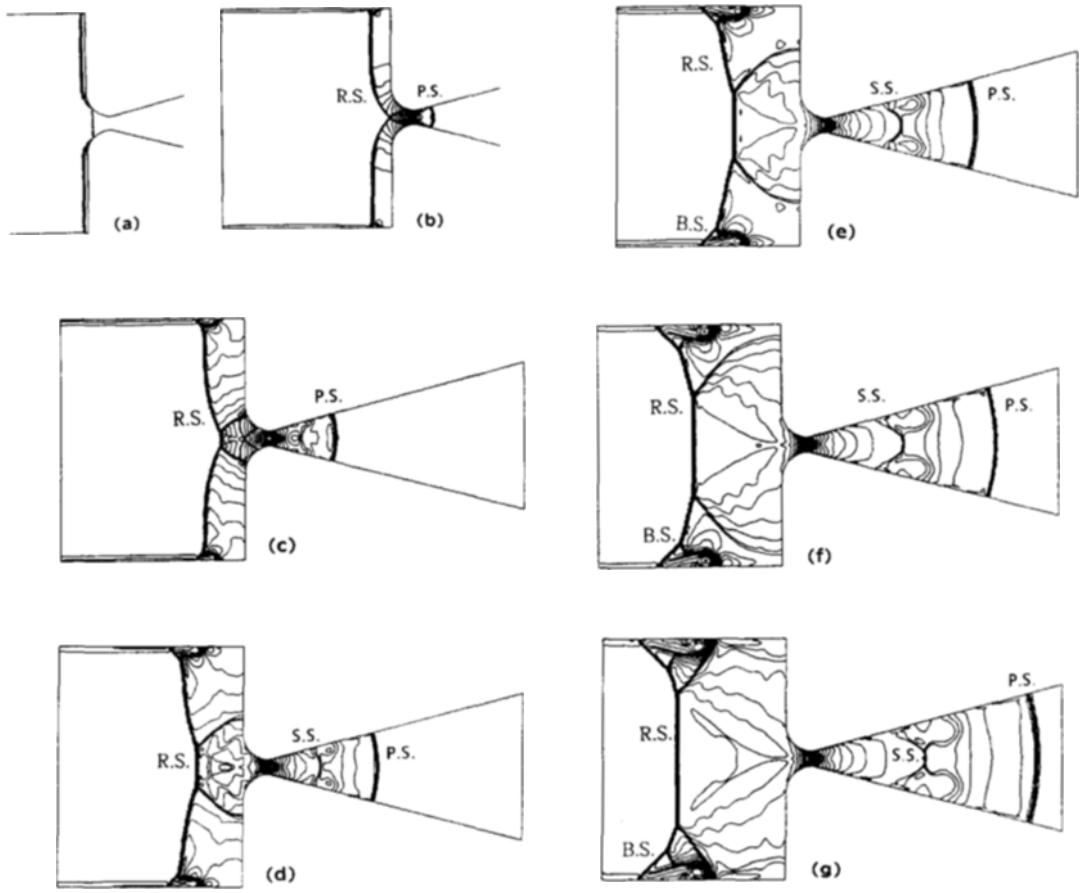

Fig. 7 Isopycnics showing transient nozzle flows induced by shock wave, $M_s=2.3$, $Re=2.5\times10^5$. (a) $t'=1.34$ (b) $t'=1.60$ (c) $t'=1.92$ (d) $t'=2.24$ (e) $t'=2.56$ (f) $t'=2.87$ (g) $t'=3.19$

plane between the two instants is $\Delta t'=0.32$, which is equivalent to $\Delta t=0.021$ msec in a physical plane. From this comparison, the present numerical results simulated the wave propagation velocity fairly well.

4.2 Unsteady shock waves in nozzle *B*

The computational results for nozzle B (Fig. 1(b)) are shown in Fig. 7. The geometry of the nozzle B is : throat radius=17mm, throat length =10mm, half angle=15°, nozzle length=180 mm. The incident shock Mach number is $M_s=2.3$ and the Reynolds number is 2.5×10^5. Since the normalized throat length of the nozzle B is considerably narrow compared to the nozzle A, the computational domain is divided into two regions to avoid the potential numerical error due to excessive grid skewness. The two regions are the region near the side wall of the shock tube section and the remaining region, respectively. As the numerical grid system, the two-block grid with 120×90 and 300×30 grid points is generated.

Figure 7 represents the time evolution of unsteady flowfield induced by shock waves. The flowfields are shown as the series of isopycnics. the shock wave structures are essentially same to those in the nozzle A. At $t'=1.34$, The incident shock reflects from the nozzle throat and shows regular reflection. The upstream-facing reflected shock (R.S.) represents regular reflection at $t'=1.60$ and transits to Mach reflection at $t'=1.92$. In Fig. 7(d), the secondary shock wave (S.S.) is

observed. The shape of the upstream-facing secondary shock is slightly different from those shown in Fig. 3. The front of the secondary shock is convex toward the nozzle throat (Fig.7(e) to (g)). This is due to the interaction of secondary shock with the boundary layer developed in the nozzle wall. The secondary shock system, therefore, becomes the structure with the front-leg and rear-limb shocks. This shock structure is similar to that of the bifurcated shock reflected from the end wall of shock tube. The bifurcated shock (B.S.) is shown in the side wall region of the shock tube section(Fig. 7(e) to (g))

4.3 Transient flows around an aerodynamic-model

We have also conducted some numerical calculations to examine the transient flow process around an airfoil model installed inside the nozzle. Thus the flow establishment process and shock wave propagation behavior around the aerodynamic model are numerically investigated. The two-dimensional airfoil of NACA 0012 is used as the aerodynamic model. The calculation conditions in this case are $M_s=3.2$ and $Re=5\times10^5$. The leading edge of the airfoil is placed at $x/L=5.04$ and the normalized cord length is $c'=0.5(c'=c/L)$. The airfoil installed has a zero angle of attack.

In Fig. 8, the time course of flowfields are shown as computer shadowgraphs. In Fig. 8(a), the primary shock wave (P.S.) has just passed over the airfoil model and a new shock wave is formed at the leading edge. In addition, a secondary shock wave (S.S.) is clearly identified and is found to be approaching the model. At $t'=1.97$ (Fig.8(b)), the model is located between the primary and secondary shock waves, so that the flow around the model is not yet steady. Then the secondary shock ware reaches the model and merges with the shock wave at the leading edge, as shown in Fig. 8(c). A recompression shock wave is observed in the vicinity of the trailing edge (indicated as arrow in Fig. 8(c)). Figure 8(d) indicates that a steady nozzle flow has been established. It can be seen that the flow is greatly separated from the wall, and a separation shock

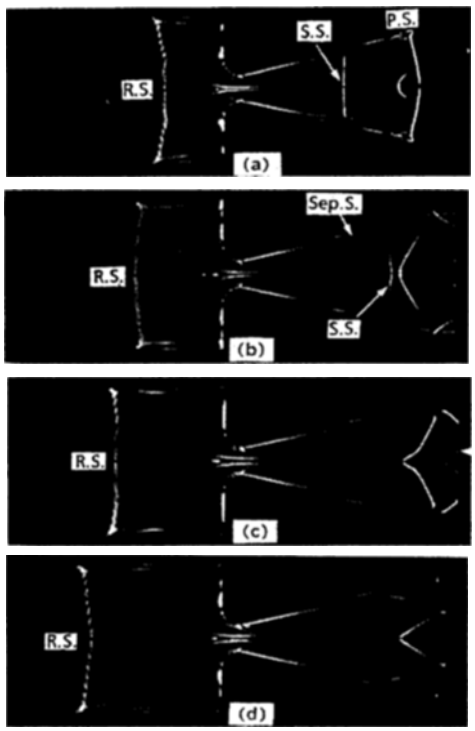

Fig. 8 Computer shadowgraphs showing transient flows around aerodynamic model M_s 3.2 (a) t' 1.66 (b) t' 1.97 (c) t' 3.28 (d) t' 2.59

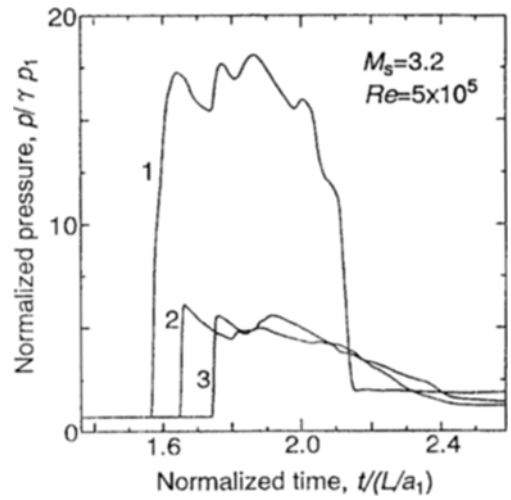

Fig. 9 Time variations of static pressure on three points of model surface

wave is generated. This separation shock wave interacts with the shock generated from the leading edge of the airfoil. A simple theory assuming an isentropic expansion predicts the flow Mach
number of M_e=2.39 at the nozzle exit.

The time variations of a static pressure on the model surface are presented in Fig.9. The numbers in the figure mean 1: leading edge (x/L=5.04), 2: upper surface (x/L=5.29), and 3: trailing edge (x/L=5.54). At t'=1.56, the jump of the pressure monitored at the leading edge denotes the passing of a primary shock wave. After the transient variation, the pressure at the leading edge (1) approaches a steady value at t'=2.16. The first pressure jumps at the model surface (2) and the trailing edge (3) also indicates the passing of the primary shock wave. The quasi-steady flows around the airfoil are established at t'=2.52.

5. Conclusions

The unsteady starting process of nozzles installed in a shock tube has been investigated numerically and experimentally. Computer shadowgraphs have been developed for the purpose of understanding the transient flow structure in the nozzle. Satisfactory agreement between numerical and experimental results was obtained. In addition, numerical simulations were conducted to examine the steady flow establishment process around an airfoil model installed inside the nozzle. The simulated results successfully revealed the unsteady viscous flow structure around the model.

Reference

Amann, H. O. and Reichenbach, H., 1973, "Unsteady Flow Phenomena in Shock Tube Nozzles," *Recent Developments in Shock Tube Research*,(Bershader, D., and Griffith, W. eds.), p. 96, Stanford Univ. Press.

H. C. Yee, 1989, "A Class of High-Resolution Explicit and Implicit Shock-Capturing Methods," *NASA Technical Memorandum* 101088, p. 101

Harten, A., 1983, "High Resolution Schemes for Hyperbolic Conservation Laws," *J. Comput. Phys.*, Vol. 49, p. 357.

Hertzberg, A., 1951, "A Shock Tube Method of Generating Hypersonic Flows," *J. Aero. Sci.*, Vol. 18, p. 803.

Holden, M. S., 1971, "Establishment Time of Laminar Separated Flows," *AIAA J.*, Vol. 9, p. 2296.

Ikui, T. and Matsuo, K., 1971, "A Study on Aerodynamic Characteristics of Shock Tube," *Trans. Jpn. Soc. Mech. Eng.*, Vol. 37, p. 1536.

Jacobs P. A., 1992, "Simulation of Transient Flow in a Shock Tunnel and a High Mach Number Nozzle," *Proc. 4th Int. Symp. Comput. Fluid Dynamics*, Davis, USA, p. 533.

Kashimura, H., Iwata, N. and Nishida, M., 1986, "Numerical Analysis of the Wave Propagation in a Duct with an Area Change by Random Choice Method," *Bulletin of JSME*. Vol. 29, p. 1440.

Lee, M. G. 1995, *Propagation Behavior of Unsteady Shock Waves*, Dr. Eng. Dissertation of Graduate School, Kyushu University

Lee, M. G. and M. Nishida, 1993, "Computational Study on Shock Wave Propagation and Starting Process in a Shock Tunnel Nozzle." *Proc. 5th Int. Symp. Comput. Fluid Dynamics*, Sendai, Japan, Vol. 2, p. 120.

Lee, M. G. and Nishida, M., 1992, "Computation of an Unsteady Starting Process in a Hypersonic Nozzle," *Proc. 5th Asian Congress of Fluid Mechanics*, Taejeon, Korea, Vol. 2, p. 948.

Miyashiro, S., Kleine, H. and Gronig, H., 1992, "Novel Nanosecond Spark Source for Optical Measurements in Shock Wave Research," *Shock Waves* (Takayama, K., ed.), p. 973, Springer-Verlag

Nishida, M. and Lee, M. G., 1994, "Propagation Behavior of Strong Shock Waves with Chemical Reactions in a Shock Tunnel Nozzle," *Proc. 19th Int. Symp. Shock Waves*, Marseille, France, p. 301, Springer-Verlag.

Prodromou, P. and Hiller, R., 1992, "Computation of Unsteady Nozzle Flow," *Shock Waves* (Takayama, K. ed.), p. 1113, Springer-Verlag.

Smith, C. E., 1966, "The Starting Process in a Hypersonic Nozzle," *J. Fluid Mech.*, Vol. 24, p. 625.

Steger, J. L. and Sorenson, R. L., 1979, "Automatic Mesh-Point Clustering near a Boundary in Grid Generation with Elliptic Partial Differential Equation," *J. Comput. Phys.*, Vol 33, p. 405.

Takeishi, K., Matsuura, M., Sakamura, Y., Lee, M. G. and Nishida, M., 1994, "Large-Scale Shock Tunnel and Its Instrumentation," *J. Jpn. Soc. Aero. Space Sci.*, Vol 42, NO. 482, p. 135.

Wittliff, C. E., Wilson, M. R. and Hertzberg, A., 1959, "The Tailored-Interface Hypersonic Shock Tunnel," *J. Aero. Sci.*, Vol. 26, p. 219.

Yee, H. C., 1989, "A Class of High-Resolution Explicit and Implicit Shock Capturing Methods," *NASA Technical Memorandum* 101088.